energies
MDPI

Article

A New ZVS Tuning Method for Double-Sided LCC Compensated Wireless Power Transfer System

Sizhao Lu, Xiaoting Deng, Wenbin Shu, Xiaochao Wei and Siqi Li *

Faculty of Electric Power Engineering, Kunming University of Science of Technology, Kunming 650500, China; lusz10@kmust.edu.cn (S.L.); dengxiaoting2628@126.com (X.D.); wenbinshu@foxmail.com (W.S.); viva1117@163.com (X.W.)
* Correspondence: lisiqi@kmust.edu.cn; Tel.: +86-186-8717-6365

Received: 31 December 2017; Accepted: 22 January 2018; Published: 1 February 2018

Abstract: This paper presents a new zero voltage switching (ZVS) tuning method for the double-sided inductor/capacitor/capacitor (LCC) compensated wireless power transfer (WPT) system. An additional capacitor is added in the secondary side of the double-sided LCC compensation network in order to tune the network to realize ZVS operation for the primary-side switches. With the proposed tuning method, the turn off current of the primary-side switches at the low input voltage range can be reduced compared with the previous ZVS tuning method. Consequently, the efficiency of the WPT at the low input voltage range is improved. Moreover, the relationship between the input voltage and the output power is more linear than that of the previous ZVS tuning method. In addition, the proposed method has a lower start-up voltage. The analysis and validity of the proposed tuning method are verified by simulation and experimental results. A WPT system with up to 3.5 kW output power is built, and 95.9% overall peak efficiency is achieved.

Keywords: double-sided inductor/capacitor/capacitor (LCC); wireless power transfer (WPT); zero voltage switching (ZVS)

1. Introduction

Wireless power transfer (WPT) technology can deliver electric power over certain distances without metal-to-metal contact by utilizing energy-contained fields [1,2]. WPT has attracted more and more research interest due to its convenience, safety and other advantages [3], particularly in electric vehicle (EV) charging [4,5].

Many academic papers have been published on WPT and many aspects of WPT have been studied in order to improve the performance of the WPT [4]. Among them, the compensation circuit is essential because it can be used to tune the resonant frequency of the system, reduce the reactive power in the power electronics converter, and improve the transferred power capability and efficiency [4,6]. According to the way in which the compensation capacitors are connected to the primary and secondary coils in the compensation networks, the basic compensation topologies can be classified into four types, that is, series–series (SS), series–parallel (SP), parallel–series (PS) and parallel–parallel (PP) [6,7]. A detailed analysis of these four basic compensation topologies has been conducted in [8,9]. It was concluded in [9] that SS and SP are superior to the other two compensation topologies. However, the SP compensation circuit is easily mistuned because the primary compensated capacitance relates to the coupling coefficient [10], which means the resonant frequency is dependent on the coupling coefficient. Therefore, SS compensation topology is superior to the other three compensation topologies because its resonant frequency is independent of the coupling coefficient and the load conditions [6]. The defect of the SS compensation topology is the poor output voltage regulation capability [11], so many other compensation topologies have been proposed in order to improve the efficiency or realize other purposes [12]. In [13], an inductor/capacitor (LC) compensation network is employed for the primary side and an inductor/capacitor/inductor (LCL) resonant network is formed for WPT. However, the resonant frequency of this compensation topology is dependent on the coupling coefficient and the load conditions [6]. In [14], LC compensation networks are employed for both the primary side and the secondary side and a bidirectional power transfer is achieved. In [15], an inductor/capacitor/inductor T-type (LCL-T) resonant converter is proposed which can be treated as a current source. Its primary side current is only determined by the input voltage, so the primary side current can be easily controlled. In [16], an LCC compensation network is adopted for the primary side and a zero current switching (ZCS) is achieved by tuning the parameters of the compensation network. In [17], the LCC compensation network is applied for the secondary side, which can minimize the reactive power at the secondary side and achieve a unit power factor pickup. A double-sided LCC compensation network is proposed for the WPT in [18]. Its resonant frequency is irrelevant to the coupling coefficient and the load conditions. Meanwhile, its tuning method for realizing zero voltage switching (ZVS) is also presented in [18]. A comparison study on SS and double-sided LCC compensation topology is carried out in [6]. It is concluded that double-sided LCC compensation topology is less sensitive to the self-inductance variations, lower voltage and current stress and higher efficiency compared with the SS compensation topology. Integrated LCC compensation topologies are proposed in [10,19] in order to reduce the coil size and make the system more compact with high efficiency. In [19], a numerical method to tune the compensation network parameters for ZVS is also presented. However, the turn off currents of the primary side switches are relatively large at the low input voltage condition which lowers the efficiency of the system [18,19]. In addition, the relationship between the input voltage and the output power is not so linear in the WPT system using the ZVS tuning method proposed by [18].

For high voltage high frequency metallic oxide semiconductor field effect transistor (MOSFET) switching applications, the zero voltage turn on soft switching (ZVS) condition is very important due to the poor reverse recovery characteristics of the MOSFET's body diode [20]. At the ZVS condition, the turn on switching loss is almost zero and the turn off loss is proportional to the turn off current [21]. In most of the WPT studies, the system is simply tuned to the inductive region to realize ZVS [22,23]. The turn off currents are not accurately designed. It is important to optimize the turn off current while maintaining the ZVS condition to minimize the switching loss.

In this paper, a new ZVS tuning method for double-sided LCC-compensated WPT system is proposed. For the secondary side, an additional capacitor is added to the compensation topology in order to realize ZVS operation of the primary side switches. With the proposed ZVS tuning method, the resonant frequency of the resonant network is still irrelevant with the coupling coefficient and the load conditions. Meanwhile, the turn off current of the primary-side switches at the low input voltage range can be reduced. Consequently, the efficiency of the WPT at the low input voltage range is improved. Moreover, the relationship between the input voltage and the output power is more linear than that of the previous ZVS tuning method. The proposed new ZVS tuning method and the parameter design method are also analyzed and presented in this paper, respectively. Simulation and experimental results verify the analysis and validity of the proposed circuit and the tuning method. A WPT system with up to 3.5 kW output power and 95.9% peak efficiency is built to verify the proposed ZVS tuning method.

The remainder of this paper is organized as follows. The basic circuit structure of the double-sided LCC compensation network and the new tuning method for ZVS operation are presented in Section 2. The parameter design of the proposed new ZVS tuning method is presented in Section 3. Simulated and experimental results are presented in Section 4. The conclusions are drawn in Section 5.

2. Double-Sided LCC Compensation Network and Parameter Tuning for ZVS

2.1. Double-Sided LCC Compensation Network

Figure 1 shows the double-sided LCC compensation network and corresponding power electronics circuit components. S_1–S_4 are the primary side MOSFEs. L_{ps}, C_{pp} and C_p form the primary side compensation network. L_p is the self-inductance of the transmitting coils. M is the mutual inductance of the transmitting coil and the receiving coil. L_s represent the self-inductance of the transmitting coils. L_{ss}, C_{sp} and C_s form the secondary side compensation network. C_d is a capacitor added in order to achieve ZVS for the primary side metallic oxide semiconductor field effect transistors (MOSFEs). D_1–D_4 represent the secondary side rectifier diodes. u_{AB} is the input voltage of the primary side compensation network, which is the voltage generated by V_{in} and the switching MOSFET S_1–S_4. u_{ab} represents the output voltage of the secondary side compensation network, which is related to the output voltage V_o. The currents on L_p, L_s, L_{ps} and L_{ss} are represented by i_p, i_s, i_{Lps}, i_{Lss} as shown in the Figure 1.

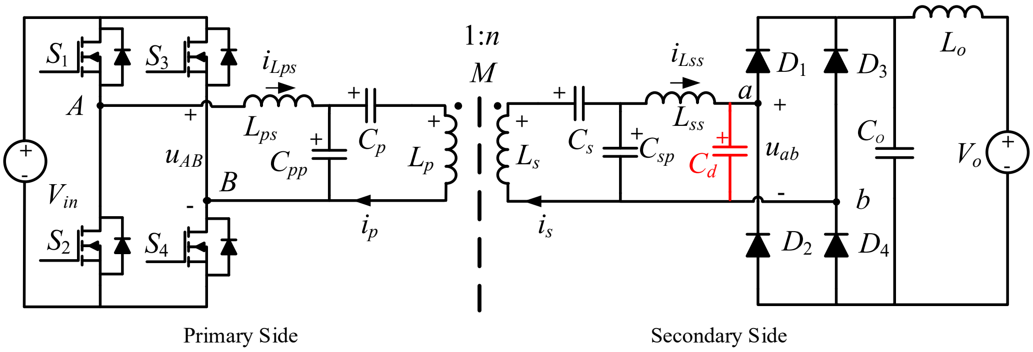

Figure 1. Double-sided inductor/capacitor/capacitor (LCC) compensation topology for wireless power transfer (WPT) system.

According to [18], the equivalent circuit to the circuit in Figure 1 referring to the primary side can be derived as shown in Figure 2; the circuit status at resonant frequency can be derived as shown in Figure 3. In Figures 2 and 3, $\mathbf{U}_{AB}$, $\mathbf{U}_{ab}$, $\mathbf{I}_P$, $\mathbf{I}_S$, $\mathbf{I}_{Lps}$, $\mathbf{I}_{Lss}$ represent the phasor form of the corresponding variables.

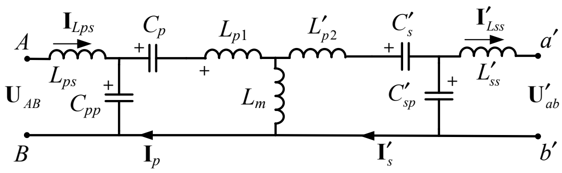

Figure 2. Equivalent circuit referring to the primary side of the proposed topology.

The variables in Figure 2 can be expressed by the following equations

$$
\begin{cases}
n = \sqrt{L_s/L_p} \\
L_m = k \cdot L_p, L_{p1} = (1-k) \cdot L_p \\
L'_{p2} = (1-k) \cdot L_s/n^2, L'_{ss} = L_{ss}/n^2 \\
C'_s = n^2 \cdot C_s, C'_{sp} = n^2 \cdot C_{sp} \\
U'_{ab} = U_{ab}/n \\
\mathbf{U}_{AB} = U_{AB}
\end{cases}
\tag{1}
$$

where k is the coupling coefficient between the transmitting and receiving coils, U_{AB} represent the root mean square value of $\mathbf{U}_{AB}$.

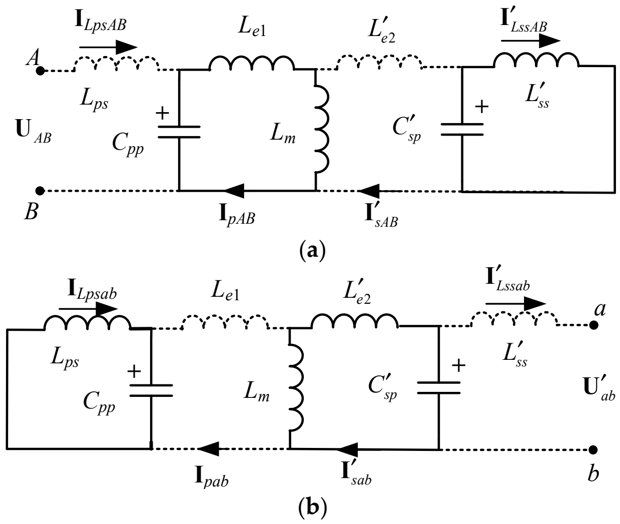

Figure 3. Circuit status at resonant frequency: (**a**) When $\mathbf{U}_{AB}$ applied only; (**b**) When $\mathbf{U}'_{ab}$ applied only.

The variables L_{e1} and L'_{e2} in Figure 3 can be expressed by the following equations

$$\begin{cases} L_{e1} = L_{ss} - k \cdot L_p \\ L'_{e2} = L'_{ps} - k \cdot L_p \end{cases} \tag{2}$$

For Equations (1) and (2), the influence of C_d is implied in $\mathbf{U}'_{ab}$. The relation between C_d and $\mathbf{U}'_{ab}$ will be analyzed in the next section. It can be seen from Figures 2 and 3 that the added C_d has no impact on the equivalent circuit of the double-sided LCC compensation network which is presented in [18]. Therefore, the similar analysis process presented in [18] can be used in this paper. However, the added C_d has impacts on $\mathbf{U}'_{ab}$, so the waveform of $\mathbf{U}'_{ab}$ in Figure 3 is different from the waveform of $\mathbf{U}'_{ab}$ in [18]. Moreover, the parameter tuning method for ZVS operation is also different.

2.2. Parameter Tuning for ZVS

For the MOSFETs, the turn off switching loss is much smaller than its turn on loss at hard switching [20]. Therefore, it is better that all the MOSFETs are turned on at ZVS conditions in order to reduce the overall switching loss. To realize ZVS for a MOSFET, the MOSFET should be turned on when the body diode is conducting. This means the resonant current of the primary side should lag the resonant voltage in order to form the ZVS operation condition for all MOSFETs. The added C_d in the secondary side of the compensation network should be properly designed in order to achieve the ZVS operation.

According to the Figure 3a,b, the following equations can be derived by superposition principle

$$\mathbf{I}'_{Lss\_1st} = \mathbf{I}'_{LssAB} + \mathbf{I}'_{Lssab} = \frac{kU_{AB}L_p}{j\omega_0 L_{ps} L'_{ss}} \tag{3}$$

$$\mathbf{I}_{Lss\_1st} = \frac{\mathbf{I}'_{Lss\_1st}}{n} = \frac{kU_{AB}\sqrt{L_p L_s}}{j\omega_0 L_{ps} L_{ss}} \tag{4}$$

where the subscript '1st' represents the first harmonic component of the corresponding item.

According to Equation (3), $\mathbf{I}_{Lss\_1st}$ leads $\mathbf{U}_{AB}$ by a phase φ_1, which can be expressed as

$$\varphi_1 = -\frac{\pi}{2} \tag{5}$$

To achieve ZVS conditions at a small turn off current, the analysis accuracy of the turn off current is very important. Therefore, the high order harmonics of the square voltage cannot be neglected. The effect of the high order harmonics current is shown in Figure 4. The phase between u_{ab} zero crossing time t_b and its maximum value time t_c is represented by a. The phase between the zero crossing of i_{Lss} and u_{ab} is represented by φ_{ab}. Meanwhile, i_{Lss} contains not only the first order current but also the high order harmonic currents. The interaction of the high order harmonics between the primary and secondary side can be neglected because the compensation networks form a high order filter between the primary side and the secondary side. Moreover, a is close to zero as shown in Figure 4, so the waveform of u_{ab} is firstly approximated by a square wave. Therefore, the high order harmonic currents of the L_{ss} can be roughly expressed as:

$$\begin{aligned} \mathbf{I}_{Lss\_3rd} &\approx -\frac{\mathbf{U}_{ab\_3rd}}{j\cdot 3\omega_0 L_{ss}+\frac{1}{j\cdot 3\omega_0 C_{sp}}} = j\frac{3\mathbf{U}_{ab\_3rd}}{8\omega_0 L_{ss}} \\ \mathbf{I}_{Lss\_5th} &\approx -\frac{\mathbf{U}_{ab\_5th}}{j\cdot 5\omega_0 L_{ss}+\frac{1}{j\cdot 5\omega_0 C_{sp}}} = j\frac{5\mathbf{U}_{ab\_5th}}{24\omega_0 L_{ss}} \\ &\cdots \\ \mathbf{I}_{Lss\_(2k+1)th} &\approx -\frac{\mathbf{U}_{ab\_(2k+1)th}}{j\cdot (2k+1)\omega_0 L_{ss}+\frac{1}{j\cdot (2k+1)\omega_0 C_{sp}}} \\ &= j\frac{(2k+1)\mathbf{U}_{ab\_(2k+1)th}}{((2k+1)^2-1)\omega_0 L_{ss}} \\ &\cdots \end{aligned} \quad (6)$$

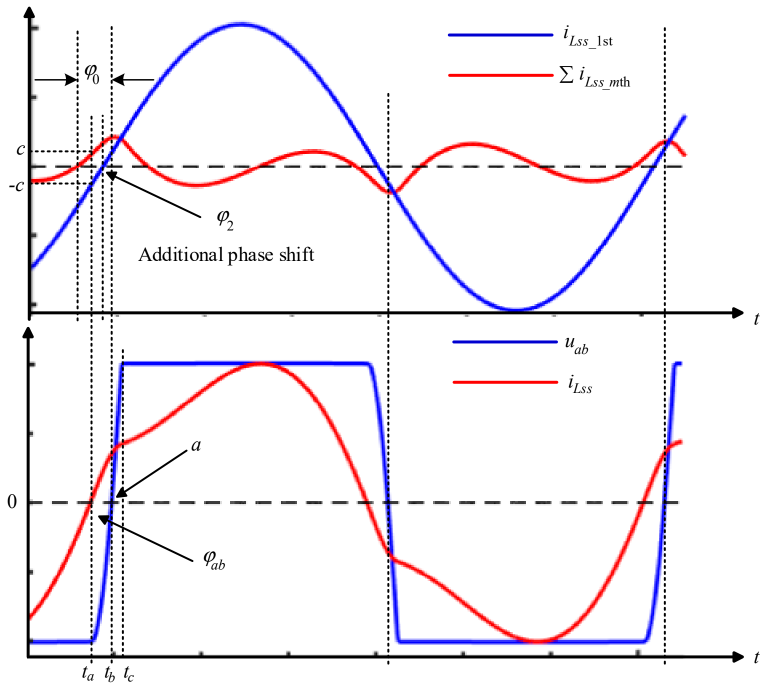

Figure 4. Effect of all high order currents.

In the time domain, the high order harmonic currents of the L_{ss} can be expressed as

$$\sum i_{Lss\_m\text{th}}(t) \approx \frac{\sqrt{2}U_{ab}}{\omega_0 L_{ss}}\left[\frac{\cos(3\omega_0 t)}{8}+\frac{\cos(5\omega_0 t)}{24}+\ldots+\frac{\cos((2k+1)\omega_0 t)}{((2k+1)^2-1)}+\ldots\right] (k=1,2,\ldots,+\infty) \quad (7)$$

According to Figure 4, the summation of all the high order harmonics is zero at $t_0 = -\varphi_0/\omega_0$,

$$\sum i_{Lss\_m\text{th}}(t)\Big|_{t=\frac{-\varphi_0}{\omega_0}} = \sum_{k=1}^{\infty} i_{Lss\_m\text{th}}(t)\Big|_{t=\frac{-\varphi_0}{\omega_0}} \approx \sum_{k=1}^{9} i_{Lss\_m\text{th}}(t)\Big|_{t=\frac{-\varphi_0}{\omega_0}} = 0 \quad (8)$$

Solve the Equation (8), then the following equation can be derived

$$\varphi_0 \approx 0.412 \tag{9}$$

According to Equation (6), $\mathbf{I}_{Lss\_m\mathrm{th}}$ leads $\mathbf{U}_{ab\_m\mathrm{th}}$ by a phase which equals to 90°. So $i_{Lss\_m\mathrm{th}}$ reaches the peak when $\mathbf{U}_{ab}$ jumps at the time t_b. The peak value of the $i_{Lss\_m\mathrm{th}}$ can be calculated by

$$\begin{aligned} \max\{\sum i_{Lss\_m\mathrm{th}}\} &= \sqrt{2}\cdot\sum_{k=1}^{\infty} I_{Lss\_(2k+1)\mathrm{th}} \\ &= \sqrt{2}\cdot\sum_{k=1}^{\infty}\frac{1}{((2k+1)^2-1)}\frac{U_{ab}}{\omega_0 L_{ss}} \\ &= \frac{\sqrt{2}}{4}\cdot\frac{U_{ab}}{\omega_0 L_{ss}} \end{aligned} \tag{10}$$

According to Equations (8)–(10), the high order harmonics can be approximated by

$$\begin{aligned} \sum i_{Lss\_m\mathrm{th}}(t) &\approx h_p + \frac{h_p\omega_0}{\varphi_0}t \\ &= \frac{\sqrt{2}}{4}\cdot\frac{U_{ab}}{\omega_0 L_{ss}}(1+\frac{\omega_0}{0.412}t) \end{aligned} \tag{11}$$

where h_p is the peak value of the total high order current.

Assuming $t_b = 0$, $t_a = -\varphi_{ab}/\omega_0$, then the following equations can be derived:

$$c = \sum i_{Lss\_m\mathrm{th}}(t_a) \approx \frac{\sqrt{2}}{4}\cdot\frac{U_{ab}}{\omega_0 L_{ss}}\left(1+\frac{\omega_0}{0.412}t_a\right) = \frac{\sqrt{2}}{4}\cdot\frac{U_{ab}}{\omega_0 L_{ss}}\left(1-\frac{\varphi_{ab}}{0.412}\right) \tag{12}$$

$$\int_{t_a}^{t_b} i_{Lss}(t)dt = \int_{\frac{-\varphi_{ab}}{\omega_0}}^{0} i_{Lss\_1\mathrm{st}}(t) + \sum i_{Lss\_m\mathrm{th}}(t)dt = C_d V_o \tag{13}$$

In Figure 4, φ_{ab} is close to zero, so $i_{Lss\_1\mathrm{st}}(t)$ in Equation (13) can be approximately expressed as

$$i_{Lss\_1\mathrm{st}}(t) = A_m t + A_m\frac{\varphi_{ab}}{\omega_0} \tag{14}$$

where

$$A_m = \frac{\sqrt{2}kU_{AB}\sqrt{L_p L_s}}{\omega_0 L_{ps} L_{ss}} \tag{15}$$

Integrating the left side of Equation (13), then the following equation can be derived:

$$\frac{1}{2}\frac{\varphi_{ab}{}^2(0.412A_m + h_p)}{0.412\omega_0} = C_d V_o \tag{16}$$

where V_o is the output voltage.

Solving the Equation (16), then the phase shift φ_{ab} can be expressed as

$$\varphi_{ab} = \sqrt{\frac{0.824C_d\omega_0 V_o}{(0.412A_m + h_p)}} \tag{17}$$

According to Figure 4, the following equation can be derived:

$$\varphi_2 \approx \varphi_{ab} - \frac{h_p(1-2.43\varphi_{ab})}{A_m} \tag{18}$$

However, the effect of the added C_d on the magnitude of h_p should be taken into consideration in order to calculate φ_2 accurately. According to Figure 4, the charge time from t_b to t_c is around 0.4 times of the charge time from t_a to t_b, so the following equations can be derived:

$$a \approx 0.4\varphi_{ab} \tag{19}$$

$$\begin{aligned} h'_p &\approx \frac{4V_o}{a\pi\omega_0 L_{ss}} \cdot \left(\frac{3}{8} \cdot \frac{1}{9}\sin(3a) + \frac{5}{24} \cdot \frac{1}{25}\sin(5a) + \ldots \frac{19}{360} \cdot \frac{1}{361}\sin(19a)\right) \\ &= \frac{8V_o}{\varphi_{ab}\pi\omega_0 L_{ss}} \cdot \left(\frac{1}{24}\sin(\frac{3\varphi_{ab}}{2}) + \frac{1}{120}\sin(\frac{5\varphi_{ab}}{2}) + \ldots \frac{1}{6840}\sin(\frac{19\varphi_{ab}}{2})\right) \end{aligned} \tag{20}$$

where h'_p is the modified peak value of the total high order current.

Substituting Equation (20) into (17), then the following equations can be derived:

$$\varphi'_{ab} = \sqrt{\frac{0.824C_d\omega_0 V_o}{\left(0.412A_m + h'_p\right)}} \tag{21}$$

$$a' \approx 0.4\varphi'_{ab} \tag{22}$$

$$h''_p \approx \frac{8V_o}{\varphi'_{ab}\pi\omega_0 L_{ss}} \cdot \left(\frac{1}{24}\sin(\frac{3\varphi'_{ab}}{2}) + \frac{1}{120}\sin(\frac{5\varphi'_{ab}}{2}) + \ldots \frac{1}{6840}\sin(\frac{19\varphi'_{ab}}{2})\right) \tag{23}$$

Finally, the phase by which i_{Lss_1st} leads u_{ab} can be obtained:

$$\varphi_2 \approx \varphi'_{ab} - \frac{h''_p(1 - 2.43\varphi'_{ab})}{A_m} \tag{24}$$

In Figure 4, $\mathbf{I}_{Lss\_1st}$ leads $\mathbf{U}_{ab}$ by a phase ϕ_2. According to Equation (5), the following equations can be derived:

$$\cos\varphi = \cos(\varphi_1 - \varphi_2) = \cos\left(-\frac{\pi}{2} - \varphi_2\right) = -\sin\varphi_2 \tag{25}$$

$$\begin{aligned} \mathbf{I}_{Lps\_1st} &= -\frac{k\mathbf{U}'_{ab}L_P}{j\omega_0 L_{ps}L'_{ss}} = -\frac{kU'_{ab}(\cos\varphi + j\cdot\sin\varphi)L_p}{j\omega_0 L_{ps}L'_{ss}} \\ &= -\frac{kU'_{ab}\sin\varphi L_p}{\omega_0 L_{ps}L'_{ss}} - \frac{kU'_{ab}\cos\varphi L_p}{j\cdot\omega_0 L_{ps}L'_{ss}} \\ &\approx \frac{kU_{ab}\sqrt{L_pL_s}}{\omega_0 L_{ps}L_{ss}} + \frac{kU_{ab}\sin\varphi_2\sqrt{L_pL_s}}{j\cdot\omega_0 L_{ps}L_{ss}} \\ &\approx \frac{kU_{ab}\sqrt{L_pL_s}}{\omega_0 L_{ps}L_{ss}} + \frac{kU_{ab}\varphi_2\sqrt{L_pL_s}}{j\cdot\omega_0 L_{ps}L_{ss}} \end{aligned} \tag{26}$$

According to [18], the total high order current peak value of the primary side can be calculated by:

$$\max\{\sum i_{Lss\_m\text{th}}\} = \frac{\sqrt{2}}{4} \cdot \frac{U_{AB}}{\omega_0 L_{ss}} \tag{27}$$

The turn off current of the MOSFET is determined by both the first order and the high order harmonic currents. According to Equations (26) and (27), the turn off current of the MOSFET can be calculated as:

$$i_{OFF} = \sqrt{2}\left(\frac{kU_{ab}\varphi_2\sqrt{L_pL_s}}{\omega_0 L_{ps}L_{ss}} + \frac{U_{AB}}{4\omega_0 L_{ps}}\right) \tag{28}$$

According to the MOSFET parameters, a minimum turn off current $I_{OFF\_\min}$ which can achieve ZVS can be determined [21]. Then,

$$i_{OFF\_\min} \le \sqrt{2}\left(\frac{kU_{ab}\varphi_2\sqrt{L_pL_s}}{\omega_0 L_{ps}L_{ss}} + \frac{U_{AB}}{4\omega_0 L_{ps}}\right) \tag{29}$$

According to Equations (21), (24) and (28), it can be seen that a turn off current can be calculated for a given C_d. When the value of C_d is increased, the phase shift φ_{ab} and φ_2 will also be increased. Consequently, the turn off current will also be increased.

3. Parameter Design

In this section, a 3.6 kW WPT system is designed according to the above analysis. The parameters of the WPT system are shown in Table 1.

Table 1. Parameters of wireless power transfer (WPT) system.

Spec/Parameter	Values
Input DC voltage	<500 V
Output voltage	300–450 V
Nominal gap	120 mm
Coupling coefficient	0.2–0.3
Transmitting coil inductance	300 µH
Transmitting coil AC resistance	~500 mΩ
Receiving coil inductance	202.7 µH
Receiving coil AC resistance	~500 mΩ
Switching frequency	85 kHz
Maximum power	~3.6 kW

If U_{AB} is not too low, Figure 4 and Equations (7)–(9) satisfies. Thus $\varphi_2 < \varphi_0/2 \approx 0.2$, and $\cos\varphi_2 \approx 1$. From Table 1 and according to the design principle for minimizing the total reactive power in L_p and L_s [24], the L_{ps} and L_{ss} can be designed as

$$\begin{aligned} L_{ps} &= U_{AB}\sqrt{\frac{k_{\max}}{\omega_0 P_{\max}} \cdot L_p} \\ &= \frac{2\sqrt{2}}{\pi} \times 500 \times \sqrt{\frac{0.3}{2\pi \times 85 \times 10^3 \times 3.6 \times 10^3} \cdot 300 \times 10^{-6} H} \\ &\approx 97.40\ \mu H \end{aligned} \tag{30}$$

$$\begin{aligned} L_{ss} &= U_{ab}\sqrt{\frac{k_{\max}}{\omega_0 P_{\max}} \cdot L_s} \\ &= \frac{2\sqrt{2}}{\pi} \times 450 \times \sqrt{\frac{0.3}{2\pi \times 85 \times 10^3 \times 3.6 \times 10^3} \cdot 202.7 \times 10^{-6} H} \\ &\approx 72.05\ \mu H \end{aligned} \tag{31}$$

The values of C_{pp} and C_{sp} can be derived from the following equations,

$$\begin{cases} C_{pp} = \frac{1}{\omega_0^2 L_{ps}} \approx 36\ nF \\ C_{sp} = \frac{1}{\omega_0^2 L_{ss}} \approx 48.66\ nF \end{cases} \tag{32}$$

The values of C_{ps} and C_{ss} can also be calculated from

$$\begin{cases} C_{ps} = \frac{1}{\omega_0^2 (L_p - L_{ps})} \approx 17.30\ nF \\ C_{ss} = \frac{1}{\omega_0^2 (L_p - L_{ss})} \approx 26.83\ nF \end{cases} \tag{33}$$

The minimum turn off current is different for different MOSFET and dead-time settings. The turn off current should be large enough to discharge the junction capacitors within the dead-time in order to achieve ZVS, which can be expressed as [21]:

$$i_{OFF} \geq \frac{4\int_0^{U_{AB,\max}} C_{oss}(u_{ds})du_{ds}}{t_d} \tag{34}$$

where $U_{AB,\max}$ is the maximum input voltage, u_{ds} is the drain-source voltage of the MOSFET, C_{oss} is the junction capacitance which is a function of u_{ds}, and t_d is the dead-time. In this paper, Cree C3M0065090D SiC MOSFET (Cree, Research Triangle Park, NC, USA) is chosen as the primary side switches. According to the MOSFET parameters from the datasheet and Equation (34), the turn off current should be larger than 1A in order to realize ZVS. Therefore, the minimum turn off current $I_{OFF\_\min}$ is designed to be 2A.

Theoretical results of the MOSFETs' turn off current $I_{\rm OFF}$ with different values of C_d are shown in Figure 5. For a given C_d, the turn off current varies as the input voltage increasing. Therefore, the selection of C_d should satisfy the minimal turn off current requirement for all the input voltage. It can be seen from the Figure 5a that the value of C_d can be designed to be 2.8 nF in order to ensure that the turn off current is larger than 2A.

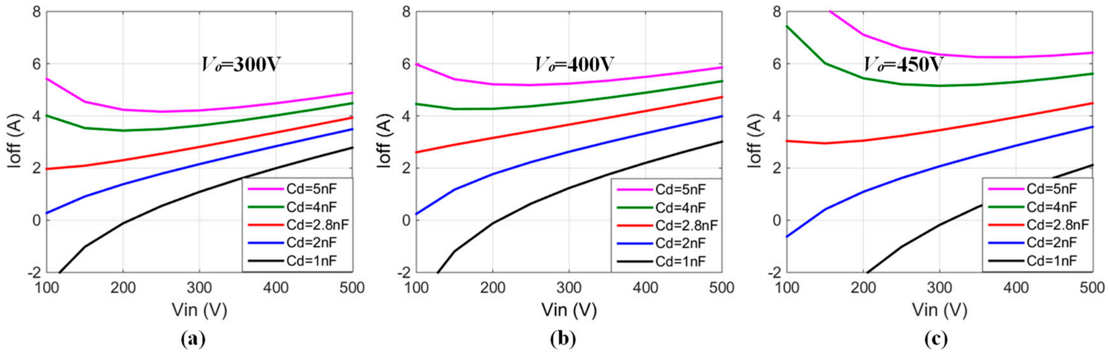

Figure 5. Theoretical calculation results of the metallic oxide semiconductor field effect transistor (MOSFET)'s turn off current $I_{\rm OFF}$ with different value of C_d: (**a**) V_o = 300 V, (**b**) V_o = 400 V and (**c**) V_o = 450 V.

According to the above calculations, the designed parameters of the compensation network is shown in Table 2.

Table 2. Parameters of compensation network.

Parameter	Values
L_{ps}	97.4 µH
L_{ss}	72.05 µH
C_{pp}	36 nF
C_{sp}	48.66 nF
C_{ps}	17.3 nF
C_{ss}	26.83 nF
C_d	2.8 nF

4. Simulation and Experimental Results

4.1. Simulated Results

To evaluate the performance of the proposed ZVS tuning method, a simulation model is built in LTspice. The parameters of the simulation model are shown in Tables 1 and 2. The various misalignments between transmitting coil and the receiving coil can be reflected by the different coupling coefficients. Therefore, three coupling coefficients, namely, k = 0.2, 0.25, 0.3, and three output voltages, V_o = 300, 400, and 450 V, are chosen as case studies in the simulations. Figure 6 shows the comparison of simulation and theoretical calculation results for the output power as a function of input voltage for three coupling coefficients and three output voltage. It can be seen from the Figure 6 that the simulation results agree well with the theoretical analysis and the output power varies linearly with the input voltage from 100 V to 500 V.

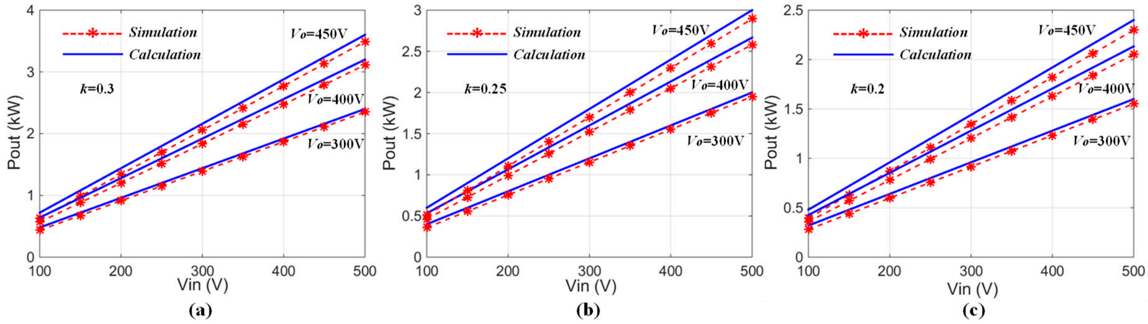

Figure 6. Simulation and theoretical calculation results of the output power for different coupling coefficients: (**a**) k = 0.3, (**b**) k = 0.25 and (**c**) k = 0.2.

Figure 7 shows the comparison of simulation and theoretical calculation results for the turn off currents as a function of input voltage for three coupling coefficients and three output voltages. It can be seen from the Figure 7 that the simulation results agree well with the theoretical analysis, which verifies the validity of the theoretical analysis.

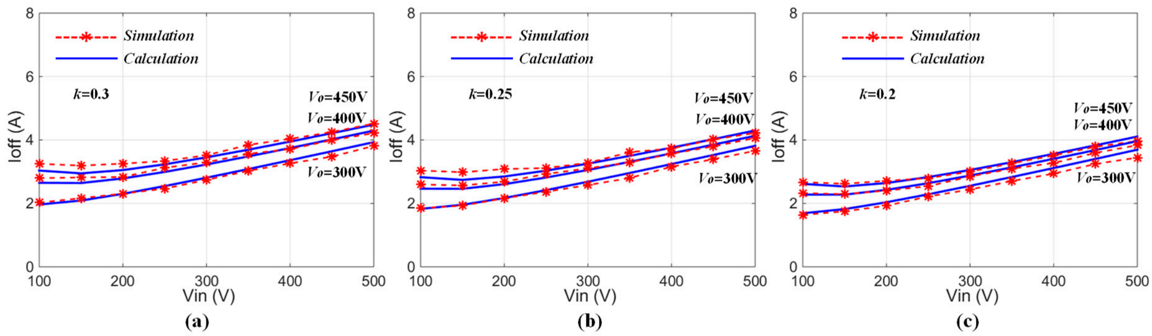

Figure 7. Simulation and theoretical calculation results of the turn off currents for different coupling coefficients: (**a**) k = 0.3, (**b**) k = 0.25 and (**c**) k = 0.2.

4.2. Experimental Results

A WPT experimental setup was built as shown in Figure 8a in order to verify the theoretical analysis and simulation results. The parameters of the prototype are tabulated in Tables 1 and 2. The widths of the transmitter coil and the receiver coil are 500 mm and 450 mm, respectively. The air gap between two coils is 120 mm. The coupling coefficient k = 0.3, and three output voltages, V_o = 300, 400, and 450 V, are chosen as the case studies in the experiment. An electronic load at constant voltage mode is used to represent the battery pack for flexible voltage adjustment. The efficiency screen shot from power meter WT1800 (Yokogawa, Tokyo, Japan) at output power of 3.5 kW is shown in Figure 8b. Urms1, Irms1 and Urms5, Irms5 represent the voltages and currents of the input side and the output side, respectively. P1 and P5 represent the input and output power, respectively. η_2 is the efficiency of the WPT system. Figure 9 shows comparison of theoretical and experimental output power as a function of input voltage for three output voltages. The experimental output power matches well with the theoretical calculation. They vary linearly with the input voltage very well even at the low input voltage. The comparison of the experimental output power of the proposed new ZVS tuning method and the previous method proposed in [18] are shown in Figure 10. The relationship between the input voltage and the output power of the proposed new ZVS tuning method is more linear than that of the previous ZVS tuning method, especially at the low input voltage conditions. Moreover, the WPT system using the previous ZVS tuning method cannot start up at V_{in} = 100 V when V_o = 400 and V_o = 450 V. This is why the output power data of the WPT system using the previous ZVS tuning method are not shown at V_{in} = 100 V in Figure 10b,c. It is obvious that the proposed new ZVS tuning method has a lower start-up voltage.

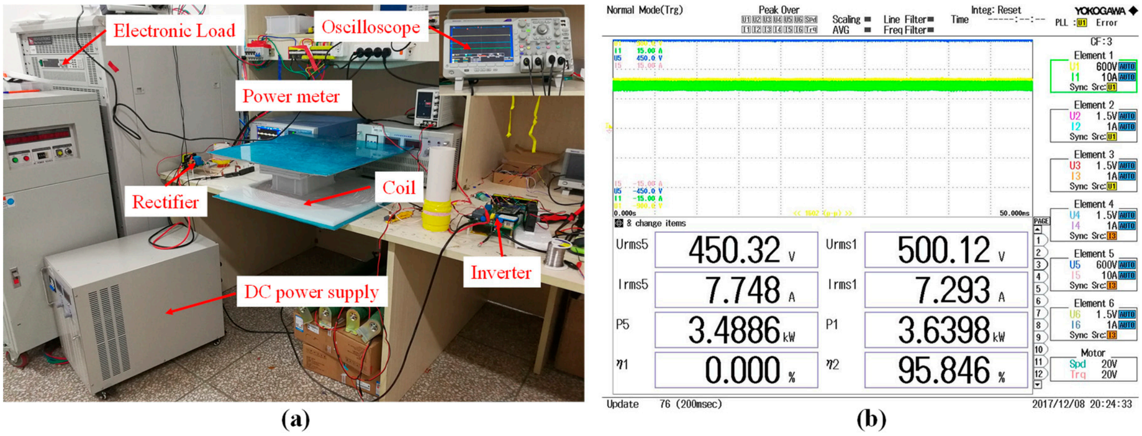

Figure 8. Experimental setup: (**a**) Picture of the experimental setup and (**b**) efficiency from power meter at output power of 3.5 kW.

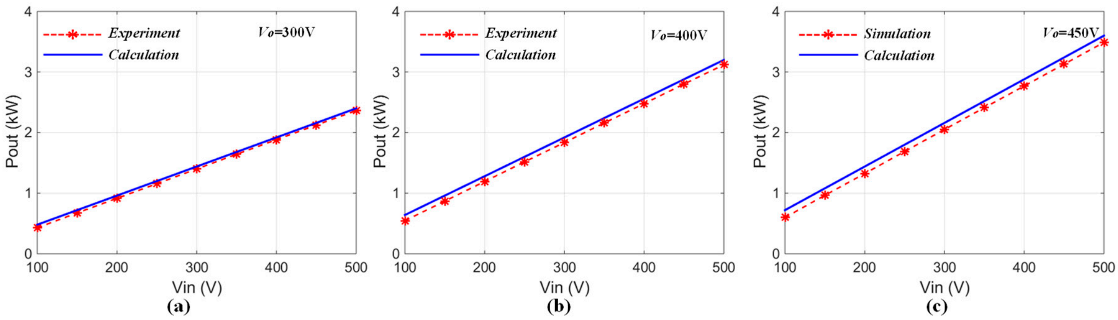

Figure 9. Theoretical calculation and experimental results of the output power for different output voltages: (**a**) V_o = 300 V, (**b**) V_o = 400 V and (**c**) V_o = 450 V.

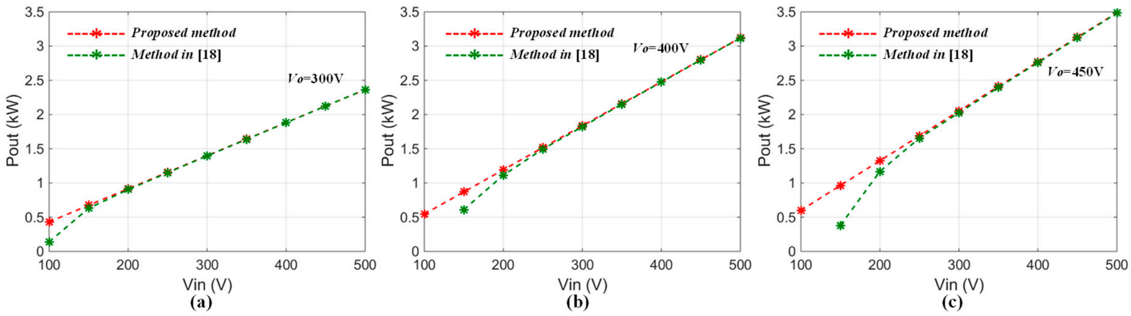

Figure 10. Experimental output power of two zero voltage switching (ZVS) tuning methods for different output voltages: (**a**) V_o = 300 V, (**b**) V_o = 400 V and (**c**) V_o = 450 V.

Figure 11 shows the theoretical calculation and experimental results of MOSFETs' turn off currents for different output voltages. The experimental results agree well with the theoretical analysis. The primary-side waveforms are shown in Figure 12 when the WPT system steadily delivers 3.5 kW to the load. At this operating point, the input voltage equals to 500 V, while the output voltage equals to 450 V. The turn off current of the MOSFET I_{OFF} equals 4.5 A and a good ZVS condition is achieved. Although the turn off current is higher than required, it is quite small compared with the peak current. The comparison of MOSFETs turn off currents for the proposed new ZVS tuning method and the previous ZVS tuning method is shown in Figure 13. It can be seen that the MOSFETs turn off currents of the proposed new ZVS tuning method are smaller those that of the previous ZVS tuning method, especially at the low input voltage conditions.

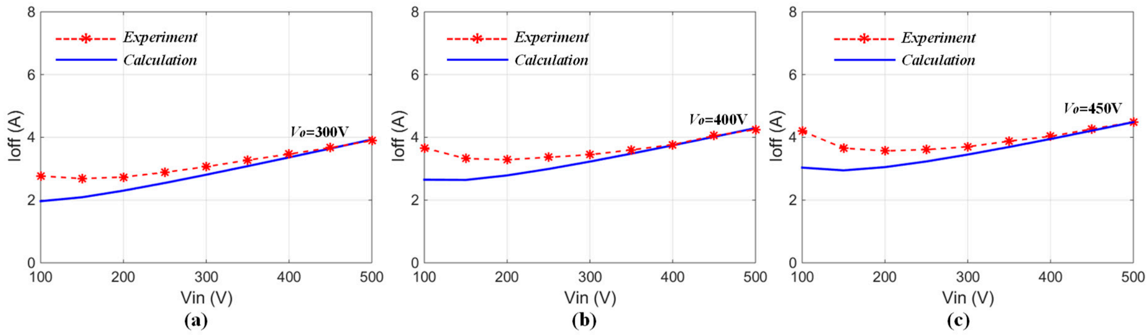

Figure 11. Theoretical calculation and experimental results of the turn off currents for different output voltages: (**a**) V_o = 300 V, (**b**) V_o = 400 V and (**c**) V_o = 450 V.

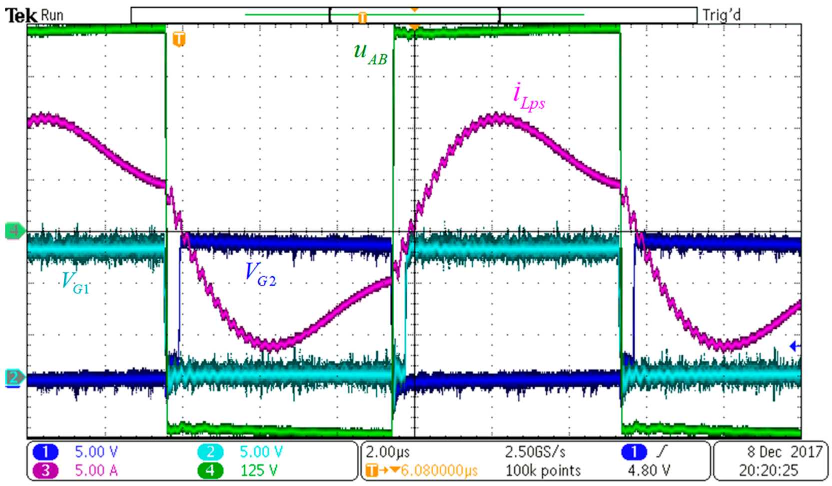

Figure 12. Waveforms of the input voltage u_{AB} and current i_{Lps} and MOSFETs gate driver signals V_{G1} and V_{G2} when delivering power of 3.5 kW. V_{in} = 500 V, and V_o = 450 V.

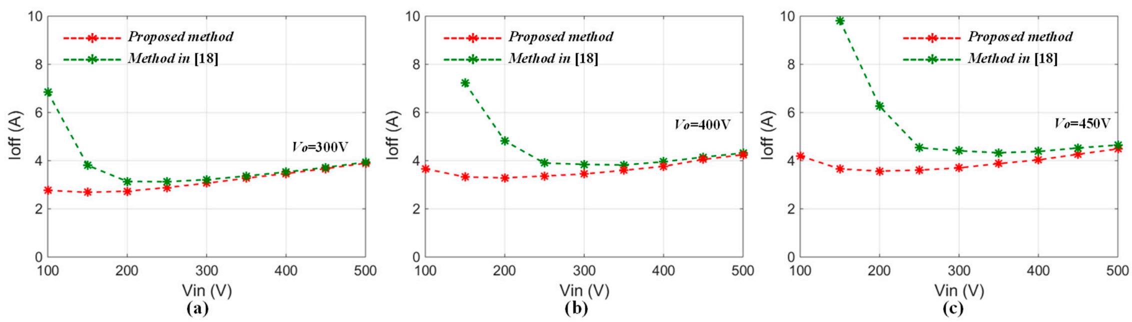

Figure 13. Experimental turn off currents of two ZVS tuning methods for different output voltages. (**a**) V_o = 300 V, (**b**) V_o = 400 V and (**c**) V_o = 450 V.

Figure 14 shows the comparison of the experimental efficiencies from the direct current (DC) power source to the battery load for the proposed new ZVS tuning method and the previous ZVS tuning method. In the experiment, an electronic load at constant voltage mode is employed to take the position of a real battery pack in order to facilitate voltage adjustment. A power meter WT1800 from Yokogawa is used to measure the efficiency of the WPT system. The maximum measured efficiency of the proposed new ZVS tuning method is 95.9% when V_{in} = 450 V, V_o = 400 V, as shown in Figure 14b. At this point, an efficiency improvement of about 0.15% is achieved compared with the previous ZVS tuning method. For the low output power range, the efficiency of these two ZVS tuning methods are almost the same when V_o = 400 V, while a significant efficiency improvement can be achieved by using the proposed new ZVS method when V_o = 300 V and V_o = 450 V. For the high output power range (>1.5 kW), the proposed new ZVS tuning method has a little higher efficiency for all the output voltages.

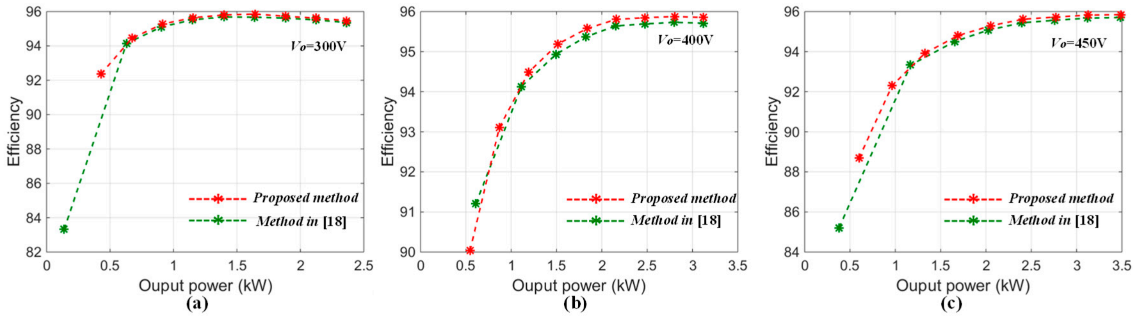

Figure 14. Experimental efficiencies of two ZVS tuning methods for different output voltages. (**a**) V_o = 300 V, (**b**) V_o = 400 V and (**c**) V_o = 450 V.

Besides the efficiency and better operations at low input voltage, the proposed method by employing C_d provides an easier, more flexible way to optimize the turn-off current. In the previous method, the resonant capacitor C_2 needs to be tuned. When the resonant capacitor and compensation inductors are integrated together with the main coils, it is very difficult to tune C_2 as it is already packed inside the coil pad [19]. Also, C_2 is in series with the main coil, which usually suffers from a much higher voltage than the output DC voltage. Sometimes C_2 is even formed by a series connected low voltage capacitors [10].

5. Conclusions

A new ZVS tuning method and its parameter design procedure for the double-sided LCC compensated WPT system is proposed in this paper. The new method ensures that the resonant frequency is irrelevant to the coupling coefficient and the load conditions, and the ZVS operation for the primary side MOSFETs is achieved. Meanwhile, the efficiency of the WPT at the low input voltage range is improved because the turn off current of the primary side switches at the low input voltage range is reduced. Moreover, a linear relationship between the input voltage and the output power is exhibited. In addition, the WPT system can start up at a lower voltage. A WPT system with output power about 3.5 kW is designed and built. Simulation and experimental results verify the analysis and validity of the proposed ZVS tuning method.

Acknowledgments: The research is supported by National Science Foundation of China (Grant Nos. 51607081 and 51707088) in part, the 5th-level talent introduction program of Kunming University of Science and Technology in part. The authors would like to thank theirs support and help. The author would also like to thank the reviewers for their corrections and helpful suggestions.

Author Contributions: Siqi Li proposed the main idea of this paper. Sizhao Lu and Xiaoting Deng contribute the circuit analysis, and completed the paper writing. Wenbin Shu and Xiaochao Wei built and tested the experimental setup.

Conflicts of Interest: The authors declare no conflict of interest.

References

1. Lu, F.; Zhang, H.; Mi, C. A Review on the Recent Development of Capacitive Wireless Power Transfer Technology. *Energies* **2017**, *10*, 1752. [CrossRef]
2. Zhang, W.; Mi, C. Compensation Topologies of High-Power Wireless Power Transfer Systems. *IEEE Trans. Veh. Technol.* **2016**, *65*, 4768–4778. [CrossRef]

3. Li, S.; Liu, Z.; Zhao, H.; Zhu, L.; Shuai, C. Wireless Power Transfer by Electric Field Resonance and Its Application in Dynamic Charging. *IEEE Trans. Ind. Electron.* **2016**, *63*, 6602–6612. [CrossRef]
4. Li, S.; Mi, C. Wireless Power Transfer for Electric Vehicle Applications. *IEEE J. Emerg. Sel. Top. Power Electron.* **2015**, *3*, 4–17.
5. Vaka, R.; Keshri, R. Review on Contactless Power Transfer for Electric Vehicle Charging. *Energies* **2017**, *10*, 636. [CrossRef]
6. Li, W.; Zhao, H.; Deng, J.; Li, S.; Mi, C. Comparison Study on SS and Double-Sided LCC Compensation Topologies for EV/PHEV Wireless Chargers. *IEEE Trans. Veh. Technol.* **2016**, *65*, 4429–4439. [CrossRef]
7. Wang, C.; Stielau, O.; Covic, G. Design considerations for a contactless electric vehicle battery charger. *IEEE Trans. Ind. Electron.* **2005**, *52*, 1308–1314. [CrossRef]
8. Khaligh, A.; Dusmez, S. Comprehensive Topological Analysis of Conductive and Inductive Charging Solutions for Plug-In Electric Vehicles. *IEEE Trans. Veh. Technol.* **2012**, *61*, 3475–3489. [CrossRef]
9. Sohn, Y.; Choi, B.; Lee, E.; Lim, G.; Cho, G.; Rim, C. General Unified Analyses of Two-Capacitor Inductive Power Transfer Systems: Equivalence of Current-Source SS and SP Compensations. *IEEE Trans. Power Electron.* **2015**, *30*, 6030–6045. [CrossRef]
10. Deng, J.; Li, W.; Nguyen, T.; Li, S.; Mi, C. Compact and Efficient Bipolar Coupler for Wireless Power Chargers: Design and Analysis. *IEEE Trans. Power Electron.* **2015**, *30*, 6130–6140. [CrossRef]
11. Cho, S.; Lee, I.; Moon, S.; Moon, G.; Kim, B.; Kim, K. Series-Series Compensated Wireless Power Transfer at Two Different Resonant Frequencies. In Proceedings of the 5th IEEE Annual International Energy Conversion Congress and Exhibition (ECCE) Asia DownUnder Conference, Melbourne, Australia, 3–6 June 2013; pp. 1052–1058.
12. Liu, X.; Clare, L.; Yuan, X.; Wang, C.; Liu, J. A Design Method for Making an LCC Compensation Two-Coil Wireless Power Transfer System More Energy Efficient Than an SS Counterpart. *Energies* **2017**, *10*, 1346. [CrossRef]
13. Wang, C.; Covic, G.; Stielau, O. Investigating an LCL load resonant inverter for inductive power transfer applications. *IEEE Trans. Power Electron.* **2004**, *19*, 995–1002. [CrossRef]
14. Madawala, U.; Thrimawithana, D. A Bidirectional Inductive Power Interface for Electric Vehicles in V2G Systems. *IEEE Trans. Ind. Electron.* **2011**, *58*, 4789–4796. [CrossRef]
15. Borage, M.; Tiwari, S.; Kotaiah, S. Analysis and design of an LCL-T resonant converter as a constant-current power supply. *IEEE Trans. Ind. Electron.* **2005**, *52*, 1547–1554. [CrossRef]
16. Pantic, Z.; Bai, S.; Lukic, S. ZCS LCC-Compensated Resonant Inverter for Inductive-Power-Transfer Application. *IEEE Trans. Ind. Electron.* **2011**, *58*, 3500–3510. [CrossRef]
17. Keeling, N.; Covic, G.; Boys, J. A Unity-Power-Factor IPT Pickup for High-Power Applications. *IEEE Trans. Ind. Electron.* **2010**, *57*, 744–751. [CrossRef]
18. Li, S.; Li, W.; Deng, J.; Nguyen, T.; Mi, C. A Double-Sided LCC Compensation Network and Its Tuning Method for Wireless Power Transfer. *IEEE Trans. Veh. Technol.* **2015**, *64*, 2261–2273. [CrossRef]
19. Li, W.; Zhao, H.; Li, S.; Deng, J.; Kan, T.; Mi, C. Integrated LCC Compensation Topology for Wireless Charger in Electric and Plug-in Electric Vehicles. *IEEE Trans. Ind. Electron.* **2015**, *62*, 4215–4225. [CrossRef]
20. Erickson, R.; Maksimovic, D. *Fundamentals of Power Electronics*, 2nd ed.; Academic: New York, NY, USA, 2001.
21. Lu, B.; Liu, W.; Liang, Y.; Lee, F. Optimal Design Methodology for LLC Resonant Converter. In Proceedings of the Twenty-First Annual IEEE Applied Power Electronics Conference and Exposition, Dallas, TX, USA, 19–23 March 2006.
22. Huh, J.; Lee, S.; Lee, W.; Cho, G.; Rim, C. Narrow-Width Inductive Power Transfer System for Online Electrical Vehicles. *IEEE Trans. Power Electron.* **2011**, *26*, 3666–3679. [CrossRef]
23. Sharp, B.; Wu, H. Asymmetrical Voltage-Cancellation Control for LCL Resonant Converters in Inductive Power Transfer Systems. In Proceedings of the 27th IEEE Applied Power Electronics Conference and Exposition (APEC), Orlando, FL, USA, 5–9 February 2012; pp. 1052–1058.
24. Luo, S.; Li, S.; Zhao, H. Reactive Power Comparison of Four-Coil, LCC and CLC Compensation Network for Wireless Power Transfer. In Proceedings of the IEEE PELS Workshop on Emerging Technologies-Wireless Power Transfer (WOW), Chongqing, China, 20–22 May 2017; pp. 268–271.